

In the previous version an error was discovered in the calculation of residual stresses, and also in the use of silica substrates. This is the corrected version, where the conclusions have changed.

Elastic Modulus of Polycrystalline Halide Perovskite Thin Films on Substrates

Madhuja Layek, Anush Ranka, In Seok Yang, Zhenghong Dai, Truong Cai,
Brian W. Sheldon, Eric Chason, and Nitin P. Padture *

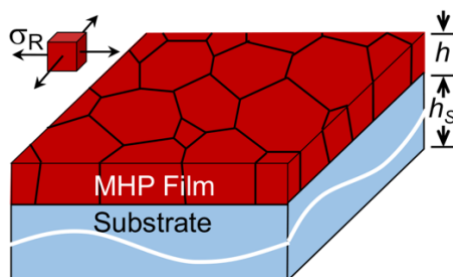
School of Engineering, Brown University, Providence, RI 02912, USA

*Email: nitin_padture@brown.edu

ABSTRACT

Using an innovative combination of multibeam-optical stress-sensor (MOSS) curvature and X-ray diffraction (XRD) techniques, the Young's modulus (E) of polycrystalline MAPbI₃ metal-halide perovskite (MHP) thin films attached to Si substrates is estimated to be 10.2±3.4 GPa. This is comparable to the E of corresponding MAPbI₃ single-crystals. This generic method could be applied to other systems to estimate hard-to-measure E of thin films.

GRAPHICAL ABSTRACT



Estimation of Young's Modulus (E) of Polycrystalline MHP (MAPbI₃) Thin Film on Si Substrate

KEYWORDS

perovskites; thin films; mechanical properties; elastic modulus; residual stress

Tremendous progress has been made in enhancing the efficiency, scalability, and operational-stability of solar cells based on metal-halide perovskites (MHPs).¹ Recently, a positive correlation between the operational-stability of perovskite solar cells (PSCs) and mechanical adhesion toughness of PSC interfaces has been demonstrated.^{2,3,4} Thus, progress is also needed in the area of mechanical reliability, a key attribute that contributes towards the overall durability of PSCs, before they can be successfully commercialized.⁵ Unfortunately, the most basic of mechanical properties, such as the Young's modulus (E) (stiffness) of MHP thin films within PSCs, are not known reliably. Methylammonium lead triiodide (CH₃NH₃PbI₃ or MAPbI₃), a 3D MHP, is the most studied by far in this regard, and the summary of its E measurements are listed in Table S1 in Supplementary Information (SI). The thin-film E values measured using techniques such as uniaxial tensile testing (free-standing thin films)⁶ and nanoindentation⁷ range widely, from 5.54 to 23 GPa. The single-crystal E values measured using uniaxial compression testing,⁸

nanoindentation,⁹ and neutron scattering¹⁰ also range widely, from 10.4 to 23.92 GPa. The reasons for these wide ranges are manifold.¹¹ Here we have measured the E of polycrystalline MAPbI₃ thin films using a new method which takes advantage of the equi-biaxial tensile residual stress (σ_R) present in these thin films when they are attached to Si substrates. The primary source of σ_R is the coefficient of thermal expansion (CTE) mismatch ($\Delta\alpha$) between the MHP thin film and the substrate, which is given by:¹²⁻¹⁴

$$\sigma_R = \frac{E\Delta\alpha\Delta T}{(1-\nu)}, \quad (\text{Eqn. 1})$$

where E and ν is the thin-film Young's modulus and Poisson's ratio, respectively, and ΔT is the difference between the heat-treatment and the use temperatures. Here we have used an innovative combination of multi-beam optical stress sensor (MOSS) curvature (Fig. 1a)¹⁴ and X-ray diffraction (XRD) $\sin^2\psi$ (Fig. 1b)¹⁵ techniques to measure E . We take advantage of the fact that the MOSS technique measures residual stress (σ_R) in the thin film, which does not require *a priori* knowledge of the thin-film E . And the XRD $\sin^2\psi$ technique measures residual strain ($\epsilon_R = \Delta\alpha\Delta T / (1-\nu)$) in the same thin films. Hooke's elasticity law, $E = \sigma_R / \epsilon_R$, is then used to estimate thin-film E , assuming in-plane biaxial isotropy.

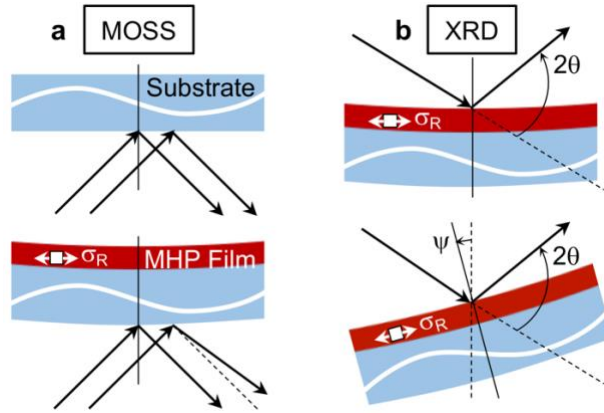


Figure 1. Schematic illustrations of:⁵ (a) MOSS and (b) XRD $\sin^2\psi$ techniques.

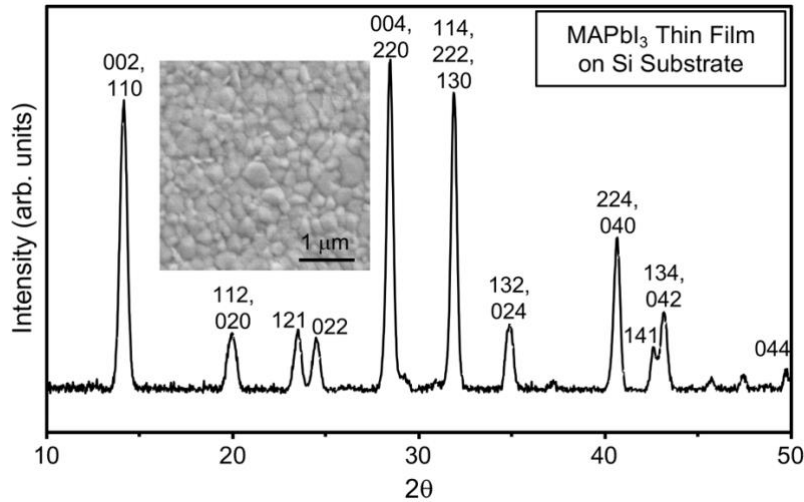


Figure 2. XRD pattern from top surface of a MAPbI₃ thin film deposited on Si substrate. Inset: top-surface SEM image of a MAPbI₃ thin film.

High-quality MAPbI₃ thin films were deposited on polished top surfaces of Si substrates, using procedures described in the SI. The average thin-film thickness is 475-500 nm. The bare backside surfaces of the Si substrates are also polished and reflective. Figure 2 presents top-surface XRD patterns of the thin films confirming pure perovskite-phase MAPbI₃. The inset in Fig. 2 is top-surface SEM image of the thin films showing a uniform, dense microstructure with an average grain size of ~225 nm. Reference curvatures of the substrates from the bottom side were measured using the MOSS technique, before and after thin-film deposition, using the procedure described in the SI. The residual strain in the very same thin films were measured using the XRD sin²ψ technique (see SI).

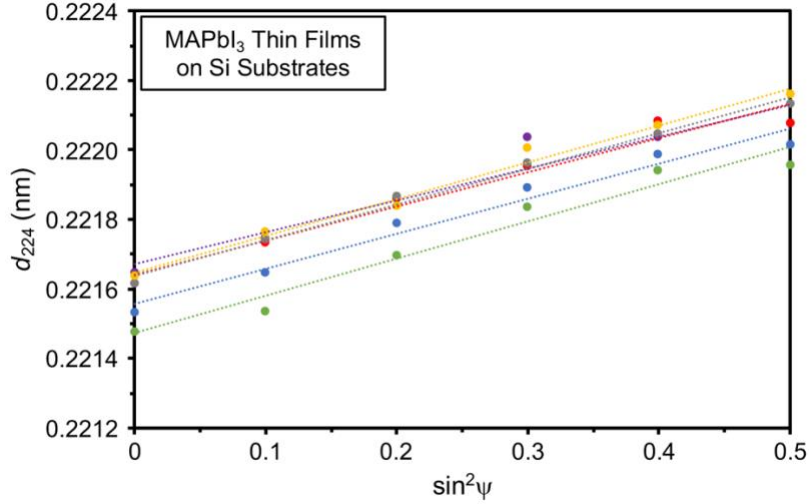


Figure 3. XRD sin²ψ measurements from MAPbI₃ thin films on Si substrates (six specimens). Dashed lines are linear fits.

The σ_R in the thin films from the steady-state MOSS curvature measurements were calculated using the Stoney equation:¹⁵

$$\sigma_R = \frac{E_S h_S^2}{6(1-\nu_S)h} \left(\frac{1}{R_C} - \frac{1}{R_0} \right), \quad (\text{Eqn. 2})$$

where E_S is the substrate Young's modulus, ν_S is the substrate Poisson's ratio, h_S is the substrate thickness, h is the film thickness, and R_0 and R_C are measured radii of curvature before and after thin-film deposition, respectively. The equi-biaxial tensile σ_R is estimated at 34.6 ± 11.5 MPa (average and standard deviation of six specimens). This average σ_R are put into the following XRD sin²ψ relation to calculate E_F of the thin film:¹⁶

$$E = (1 + \nu) \sigma_R \left(\frac{d_0}{n} \right), \quad (\text{Eqn. 3})$$

where n is the slope of fitted line to the interplanar d -spacing *vs.* sin²ψ data, and d_0 is the y -intercept. Figure 3 presents d -spacing *vs.* sin²ψ data (linear fits) for MAPbI₃ thin films on Si substrate (six specimens). The estimated E value using Eqn. 3 of MAPbI₃ thin films on Si substrate is found to be 10.2 ± 3.4 GPa. This E value, which is most relevant to PSCs because it is measured for polycrystalline thin films attached to a substrate, is comparable to single-crystal E of 10.6 ± 1.0 GPa measured in our laboratories using uniaxial compression.⁸ (Note that MOSS and XRD sin²ψ techniques were utilized by Rolston, *et al.*¹³ to measure σ_R in mixed-cation-halide MHP thin films.

However, the MOSS and the XRD $\sin^2\psi$ measurements were for thin films on Si and glass substrates, respectively. Also, no effort was made to measure E from those data in that paper.)

According to Eqn. 1, the predicted σ_R in MAPbI₃ thin film, with a CTE of $\sim 50 \times 10^{-6} \text{ }^\circ\text{C}^{-1}$ (ref. 17) on Si, with a CTE of $\sim 2.6 \times 10^{-6} \text{ }^\circ\text{C}^{-1}$ (ref. 18), for ΔT of 75 $^\circ\text{C}$ is ~ 54 MPa. This is greater than the measured average σ_R of 34.6 ± 11.5 MPa. This is possibly because the underlying assumptions in Eqn. 1 — the thin film fully attaches to the substrate only at the heat-treatment temperature and that there is no stress relaxation during cooling — may not be strictly valid. However, this is not expected to affect the E estimation.

To study the possible relaxation of the MAPbI₃ thin films at room temperature, time-dependent σ_R and ϵ_R measurements using MOSS and XRD $\sin^2\psi$, respectively, were performed, as described in the SI. Figure 4 present these data for four different specimens. While the MOSS measurements are continuous (after initial 2-3 minutes delay), each XRD $\sin^2\psi$ measurement takes ~ 12 min. The MOSS results show initial rapid (~ 12 min), but modest, relaxation in σ_R of 4-5 MPa. No appreciable relaxation in ϵ_R is observed because the XRD $\sin^2\psi$ measurement duration is relatively long. Since MOSS measurements were performed after >12 min, the E estimation above is not expected to be affected by the initial rapid stress relaxation.

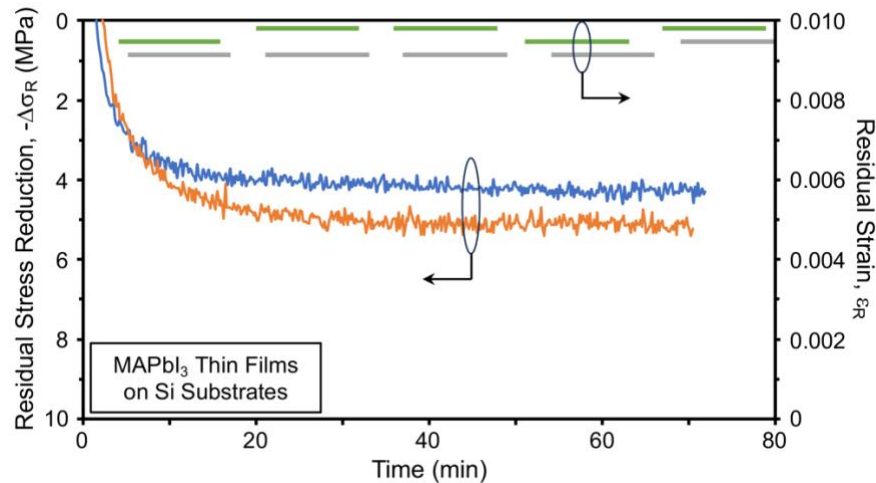


Figure 4. Time-dependent σ_R and ϵ_R measurements using MOSS and XRD $\sin^2\psi$, respectively, in MAPbI₃ thin films on Si substrates (two different specimens for σ_R and ϵ_R measurements each).

In summary, using a combination of MOSS and XRD techniques, the E of polycrystalline MAPbI₃ thin films attached to Si substrates is estimated to be 10.2 ± 3.4 GPa, which is comparable to that of corresponding E of MAPbI₃ single-crystals. This generic method could be applied to other systems to estimate hard-to-measure E of thin films.

ACKNOWLEDGEMENTS

Funding for this work was provided by the Office of Naval Research (Grant No. N00014-20-1-2574) and the National Science Foundation (Grant No. 2102210).

REFERENCES

1. Padture, N. P.: The Promise of Metal-Halide-Perovskite Solar Photovoltaics: A Brief Review. *MRS Bull.* 48, **2023**, in press (DOI: [10.1557/s4377-023-00585-6](https://doi.org/10.1557/s4377-023-00585-6)).

2. Dai, Z.; Yadavalli, S. K.; Chen, M.; Abbaspourtamijani, A.; Qi, Y.; Padture, N. P., Interfacial Toughening with Self-assembled Monolayers Enhances Perovskite Solar Cells Reliability. *Science* **2021**, *372*, 618-622.
3. Dai, Z.; Li, S.; Liu, X.; Chen, M.; Athanasiou, C. E.; Sheldon, B. W.; Gao, H.; Guo, P.; Padture, N. P., Dual-interface Reinforced Flexible Perovskite Solar Cells for Enhanced Performance and Mechanical Reliability. *Adv. Mater.* **2022**, *34* (47), 2205301.
4. Yang, I. S.; Dai, Z.; Ranka, A.; Chen, D.; Zhu, K.; Berry, J. J.; Guo, P.; Padture, N. P.: Simultaneous Enhancement of Efficiency and Operational Stability of Mesoscopic Perovskite Solar Cells *via* Interfacial Toughening. *Adv. Mater.* **2023**, in press (DOI: [10.1002/adma.202308819](https://doi.org/10.1002/adma.202308819)).
5. Dai, Z.; Padture, N. P., Challenges and Opportunities in the Mechanical Reliability of Metal-Halide Perovskites and Photovoltaics. *Nat. Energy*, **2023**, in press (DOI: 10.1038/s41560-023-01378-6).
6. Ahn, S.-M.; Jung, E. D.; Kim, S. H.; Kim, H.; Lee, S.; Song, M. H.; Kim, J.-Y., Nanomechanical Approach for Flexibility of Organic-Inorganic Hybrid Perovskite Solar Cells. *Nano Lett.* **2019**, *19*, 3707-3715.
7. Mamun, A. A.; Mohammed, Y.; Ava, T. T.; Namkoong, G., Influence of Air Degradation on Morphology, Crystal Size and Mechanical Hardness of Perovskite Film. *Mater. Lett.* **2018**, *229*, 167-170.
8. Dai, Z.; Doyle, M. C.; Liu, X.; Hu, M.; Wang, Q.; Athanasiou, C. E.; Liu, Y.; Liu, S. Z.; Sheldon, B. W.; Gao, H.; Padture, N. P., The Mechanical Behavior of Metal-Halide Perovskites: Elasticity, Plasticity, Fracture, and Creep. *Scripta Mater.* **2023**, *223*, 115064.
9. Spanopoulos, I.; Hadar, I.; Ke, W.; Tu, Q.; Chen, M.; Tsai, H.; He, Y.; Shekhawat, G.; Dravid, V. P.; Wasielewski, M. R.; Mohite, A. D.; Stoumpos, C. C.; Kanatzidis, M. G., Uniaxial Expansion of the 2D Ruddlesden-Popper Perovskite Family for Improved Environmental Stability. *J. Am. Chem. Soc.* **2019**, *141* (13), 5518-5534.
10. Ferreira, A. C.; L'etoublon, A.; Paofai, S.; Raymond, S.; Ecolivet, C.; Ruffle', B.; Cordier, S.; Katan, C.; Saidaminov, M. I.; Zhumekenov, A. A.; Bakr, O. M.; Even, J.; Bourges, P., Elastic Softness of Hybrid Lead Halide Perovskites. *Phys. Rev. Lett.* **2018**, *121*, 085502.
11. Tu, Q; Kim, D.; Shyikh, M.; Kanatzidis, M. G.: Mechanics-Coupled Stability of Metal-Halide Perovskites. *Matter* **4**, 2765 (2021).11.
12. Ramirez, C.; Yadavalli, S. K.; Garces, H. F.; Zhou, Y.; Padture, N. P., Thermo-Mechanical Behavior of Organic-Inorganic Halide Perovskites for Solar Cells. *Scripta Mater.* **2018**, *150*, 36-41.
13. Rolston, N.; Bush, K. A.; Printz, A. D.; Gold-Parker, A.; Ding, Y.; Toney, M. F.; McGehee, M. D.; Dauskardt, R. H., Engineering Stress in Perovskite Solar Cells to Improve Stability. *Adv. Energy Mater.* **2018**, *8*, 1802139.
14. Dailey, M.; Li, Y.; Printz, A. D., Residual Film Stresses in Perovskite Solar Cells: Origins, Effects, and Mitigation Strategies. *ACS Omega* **2021**, *6*, 30214-30223.
15. Chason, E.; Guduru, P. R., Tutorial: Understanding Residual Stress in Polycrystalline Thin Films Through Real-Time Measurements and Physical Models. *J. Appl. Phys.* **2016**, *119*, 191101.
16. Luo, Q.; Jones, A. H., High-precision Determination of Residual Stress of Polycrystalline Coatings using Optimised XRD- $\sin^2\psi$ Technique. *Surf. Coat. Technol.* **2010**, *205*, 1403-1408.
17. Jacobsson, T. J.; Schwan, L.J.; Ottosson, M.; Hagfeldt, A.; Edvinsson, T.: Determination of Thermal Expansion Coefficients and Locating the Temperature-Induced Phase Transition in

- Methylammonium Lead Perovskites Using X-ray Diffraction. *Inorg. Chem.* **54**, 10678 (2015).
18. Bartl, G.; Elster, C.; Martin, J.; Schödel, R.; Voigt, M.; Walkov, A.: Thermal Expansion and Compressibility of Single-Crystal Silicon Between 285 K and 320 K. *Measur. Sci. Technol.* **31**, 065013 (2020).

SUPPLEMENTARY INFORMATION

Supplementary Table

Table S1. MAPbI₃ Young's modulus (*E*) experimental values reported in the literature.

<i>E</i> (GPa)	Measurement Technique	Form	Reference
10.2±3.4	XRD + MOSS	Thin Film	This work
13.5	Nanoindentation	Thin Film	S5
19.65±2.45	Nanoindentation	Thin Film	S6
23	Nanoindentation	Thin Film	S7
8.6 - 24.6	Nanoindentation	Thin Film	S8
11.3 - 18.8	Nanoindentation	Thin Film	S9
16.5±2.0	Nanoindentation	Thin Film	S10
17.7±1.9	Nanoindentation	Thin Film	S11
22.8±3.1	Nanoindentation	Thin Film	S12
10.9	Atomic Force Microscopy	Thin Film	S13
5.54±0.73	Direct Uniaxial Tension	Free-Standing Thin Film	S14
10.4±0.8	Nanoindentation	Single-Crystal	S15
14.3±1.7	Nanoindentation	Single-Crystal	S16
10.8±2.7	Nanoindentation	Single-Crystal	S17
20.0±1.5	Nanoindentation	Single-Crystal	S18
12.7 - 17.8	Nanoindentation	Single-Crystal	S19
23.92±3.63	Nanoindentation	Single-Crystal	S20
12.6	Nanoindentation	Single-Crystal	S21
12	Nanoindentation	Single-Crystal	S22
18.9	Atomic Force Microscopy	Single-Crystal	S21
14.1	Neutron Scattering	Single-Crystal	S23
10.6±1.0	Direct Uniaxial Compression	Single-Crystal	S24

Experimental Procedure

Materials and Thin Film Preparation

MAPbI₃ precursor solution was prepared by dissolving methylammonium iodide (MAI; Greatcell, Australia) and Pb(II) iodide (PbI₂; 99.99%, TCI) in stoichiometric (1:1) ratio in a mixed solvent of 9:1 volume ratio of N,N-dimethylformamide (DMF; 99.8%, Sigma-Aldrich, USA) and dimethyl sulfoxide (DMSO; 99.7%, Sigma-Aldrich, USA) in a N₂-filled glovebox. Double-side polished Si <100> wafers with 0.2 mm thickness and 25.4 mm diameter (University Wafer, USA) were used as substrates. The polished surfaces had thermally grown oxide (~300 nm thickness) on each side. The substrates were cleaned sequentially in ultrasonic baths of detergent solution, DI water, acetone, and isopropanol. They were subsequently UV-ozone treated for 20 min before thin-film deposition. The MAPbI₃ thin films (475-500 nm thickness) were deposited on the pre-cleaned

substrates by spin-coating the precursor solution at 4,000 rpm for 20 s. Diethyl ether (Sigma Aldrich, USA) antisolvent (250 μL) was dripped at the center of the film after 10 s of spinning. The as-deposited films were then annealed at 100 $^{\circ}\text{C}$ for 10 min on a hot-plate. All the thin films were prepared in a humidity controlled dry-box (11% RH).

Characterization

The top-surfaces of the MAPbI_3 thin films were observed using a scanning electron microscope (SEM; Quattro ESEM, ThermoFisher Scientific, USA). The linear-intercept method was used on representative SEM micrographs to determine the grain sizes of the MAPbI_3 thin films. The naturally formed grooves between grains were assumed to represent the grain boundaries.

X-ray diffraction (XRD) was performed to confirm the phase purity of all the MAPbI_3 thin using a 2D diffractometer (Cu $\text{K}\alpha$ radiation; Discovery D8, Bruker, Germany) in air.

Mechanical Properties Measurement

XRD $\sin^2\psi$: Using the well-established and internally-consistent XRD $\sin^2\psi$ method the equi-biaxial tensile strains (ϵ_{R}) in the MAPbI_3 thin films were determined using six different specimens in air. The (224) Bragg reflection in the XRD pattern was used. The following relation was applied:^{S1}

$$\epsilon_{\text{R}} = \frac{n}{(1+\nu)d_0}, \quad (\text{Eqn. S1})$$

where n is the slope of the linear fits to the (224) interplanar spacing d_{224} vs. $\sin^2\psi$ data, d_0 is d spacing at $\psi = 0$ (y -intercept), and ν is the MAPbI_3 Poisson's ratio. XRD patterns at different ψ angles (0° to 45°) were collected and the systematic shift in the (224) peak position was used to generate the d_{224} vs. $\sin^2\psi$ plots. An ν value of 0.33 was used.^{S2} Typical measurement on one specimen takes ~ 12 minutes. To study any relaxation in the thin films, the ϵ_{R} values were measured as a function of time on two different specimens.

Multi-Beam Optical Stress Sensor (MOSS): The MOSS (k-Space, USA) technique was employed to measure the residual stress (σ_{R}) in the MAPbI_3 thin films in air by measuring the change of curvature of the substrate before and after thin-film deposition. Substrate backside reflective surface was used to measure the change in multi-beam spacings due to the change in curvatures. The position and the alignment of the samples were carefully monitored while measuring the change of curvature. The steady-state curvature measurements were performed ~ 12 min after the deposition was complete, and average from the first 60 s of curvature-change measurements were used for subsequent calculations. The Stoney equation (Eqn. 2) was used to calculate the thin film stress from the change in film curvature.^{S3} Average E_{S} and ν_{S} values of 150 GPa and 0.17 for Si,^{S4} respectively, were used. To study any relaxation in the thin films, the σ_{R} values were measured continuously (~ 2 minutes after the thin film processing was complete) as a function of time on two different specimens.

Supplementary References

- S1. Luo, Q.; Jones, A. H., High-Precision Determination of Residual Stress of Polycrystalline Coatings Using Optimised XRD- $\sin^2\psi$ technique. *Surf. Coat. Technol.* **2010**, *205*, 1403-1408.
- S2. Feng, J., Mechanical Properties of Hybrid Organic-Inorganic $\text{CH}_3\text{NH}_3\text{BX}_3$ (B = Sn, Pb; X = Br, I) Perovskite Solar Cell Absorbers. *APL Mater.* **2014**, *2*, 081801.

- S3. Chason, E.; Guduru, P. R., Tutorial: Understanding Residual Stress in Polycrystalline Thin Films through Real-time Measurements and Physical Models. *J. Appl. Phys.* **2016**, *119*, 191101.
- S4. Hopcroft, M. A.; Nix, W. D.; Kenny, T. W.: What is the Young's Modulus of Silicon? *J. MEMS*, **2010**, *19*, 229-238.
- S5. Park, M.; Kim, H. J.; Jeong, I.; Lee, J.; Lee, H.; Son, H. J.; Kim, D.-E., Mechanically Recoverable and Highly Efficient Perovskite Solar Cells: Investigation of Intrinsic Flexibility of Organic–Inorganic Perovskite. *Adv. Energy Mater.* **2015**, *5*, 1501406.
- S6. Mamun, A. A.; Mohammed, Y.; Ava, T. T.; Namkoong, G., Influence of Air Degradation on Morphology, Crystal Size and Mechanical Hardness of Perovskite Film. *Mater. Lett.* **2018**, *229*, 167-170.
- S7. Saraf, R.; Tsui, T.; Maheshwari, V., Modulation of Mechanical Properties and Stable Light Energy Harvesting by Poling in Polymer Integrated Perovskite Films: A Wide range, Linear and Highly Sensitive Tactile Sensor. *J. Mater. Chem. A* **2019**, *7*, 14192-14198.
- S8. Kim, D. B.; Lee, J. W.; Cho, Y. S., Anisotropic *In Situ* Strain-Engineered Halide Perovskites for High Mechanical Flexibility. *Adv. Funct. Mater.* **2021**, *31*, 2007131.
- S9. Finkenauer, B. P.; Gao, Y.; Wang, X.; Tian, Y.; Wei, Z.; Zhu, C.; D.J.Rokke; Jin, L.; Meng, L.; Yang, Y.; Huang, L.; Zhao, K.; Dou, L., Mechanically Robust and Self-Healable Perovskite Solar Cells. *Cell Rep. Phys. Sci.* **2021**, *2*, 100320.
- S10. Rathore, S.; Han, G.; Kumar, A.; Leong, W. L.; Singh, A., Elastic Modulus Tailoring in $\text{CH}_3\text{NH}_3\text{PbI}_3$ Perovskite System by the Introduction of Two Dimensionality Using $(5\text{-AVA})_2\text{PbI}_4$. *Solar Energy* **2021**, *224*, 27-34.
- S11. Gupta, Y.; Rathore, S.; Singh, A.; Kumar, A., Tailoring the Mechanical Response of Ruddlesden Popper Lead halide Perovskites. *J. Alloy. Compnd.* **2022**, *901*, 163575.
- S12. Rathore, S.; Leong, W. L.; Singh, A., Mechanical Properties Estimation of 2D-3D Mixed Organic-Inorganic Perovskites Based on Methylammonium and Phenylethyl-Ammonium System Using a Combined Experimental and First-Principles Approach. *J. Alloy. Compnd.* **2023**, *936*, 168328.
- S13. Liao, W.-C.; Liu, B. H.; Leu, C.-C., Photodegradation Pathways of $\text{CH}_3\text{NH}_3\text{PbI}_3$ Organic Perovskite Polycrystalline Film Observed by *In-situ* Scanning Probe Microscopy. *Appl. Surf. Sci.* **2021**, *545*, 149081.
- S14. Ahn, S.-M.; Jung, E. D.; Kim, S. H.; Kim, H.; Lee, S.; Song, M. H.; Kim, J.-Y., Nanomechanical Approach for Flexibility of Organic-Inorganic Hybrid Perovskite Solar Cells. *Nano Lett.* **2019**, *19*, 3707-3715.
- S15. Sun, S.; Fang, Y.; Kieslich, G.; White, T. J.; Cheetham, A. K., Mechanical Properties of Organic-Inorganic Halide Perovskites, $\text{CH}_3\text{NH}_3\text{PbX}_3$ (X= I, Br and Cl), by Nanoindentation. *J. Mater. Chem. A* **2015**, *3*, 18450-18455.
- S16. Rakita, Y.; Cohen, S. R.; Kedem, N. K.; Hodes, G.; Cahen, D., Mechanical Properties of APbX_3 (A=Cs or CH_3NH_3 ; X=I or Br) Perovskite Single Crystals. *MRS Commun.* **2015**, *5*, 623-629.
- S17. Reyes-Martinez, M. A.; Abdelhady, A. L.; Saidaminov, M. I.; Chung, D. Y.; Bakr, O. K.; Kanatzidis, M. G.; Soboyejo, W. O.; Loo, Y.-L., Time-Dependent Mechanical Response of APbX_3 (A=Cs, CH_3NH_3 ; X=I, Br) Single Crystals. *Adv. Mater.* **2017**, *29*, 1606556.
- S18. Spina, M.; Karimi, A.; Andreoni, W.; Pignedoli, C. A.; Nafradi, B.; Forro, L.; Horvath, E., Mechanical Signatures of Degradation of the Photovoltaic Perovskite $\text{CH}_3\text{NH}_3\text{PbI}_3$ Upon Water Vapor Exposure. *Appl. Phys. Lett.* **2017**, *110*, 121903.

- S19. Ramirez, C.; Yadavalli, S. K.; Garces, H. F.; Zhou, Y.; Padture, N. P., Thermo-Mechanical Behavior of Organic-Inorganic Halide Perovskites for Solar Cells. *Scripta Mater.* **2018**, *150*, 36-41.
- S20. Spanopoulos, I.; Hadar, I.; Ke, W.; Tu, Q.; Chen, M.; Tsai, H.; He, Y.; Shekhawat, G.; Dravid, V. P.; Wasielewski, M. R.; Mohite, A. D.; Stoumpos, C. C.; Kanatzidis, M. G., Uniaxial Expansion of the 2D Ruddlesden-Popper Perovskite Family for Improved Environmental Stability. *J. Am. Chem. Soc.* **2019**, *141*, 5518-5534.
- S21. Buchine, I.; Rosen-Goldian, I.; Jasti, N. P.; Ceratti, D. R.; Kumar, S.; Cahen, D.; Cohen, S. R., Nanomechanical Signatures of Degradation-free Influence of Water on Halide Perovskite Mechanics. *Nat. Commun.* **2022**, *3*, 70.
- S22. Ma, L.; Li, W.; Yang, K.; Bi, J.; Feng, J.; Zhang, J.; Yan, Z.; Zhou, X.; Liu, C.; Ji, Y.; Huang, J. C.; Han, X., A- or X-site mixture on mechanical properties of APbX₃ perovskite single crystals. *APL Mater.* **2021**, *9*, 041112.
- S23. Ferreira, A. C.; L'etoublon, A.; Paofai, S.; Raymond, S.; Ecolivet, C.; Ruffle', B.; Cordier, S.; Katan, C.; Saidaminov, M. I.; Zhumekenov, A. A.; Bakr, O. M.; Even, J.; Bourges, P., Elastic Softness of Hybrid Lead Halide Perovskites. *Phys. Rev. Lett.* **2018**, *121*, 085502.
- S24. Dai, Z.; Doyle, M. C.; Liu, X.; Hu, M.; Wang, Q.; Athanasiou, C. E.; Liu, Y.; Liu, S. Z.; Sheldon, B. W.; Gao, H.; Padture, N. P., The Mechanical Behavior of Metal-Halide Perovskites: Elasticity, Plasticity, Fracture, and Creep. *Scripta Mater.* **2023**, *223*, 115064.